

In-Situ X-ray Diffraction and STM Studies of Bromide Adsorption on Au(111) Electrodes

O. M. Magnussen*[†] and B. M. Ocko*

Department of Physics, Brookhaven National Laboratory, Upton, New York 11973

J. X. Wang and R. R. Adzic

Department of Applied Science, Brookhaven National Laboratory, Upton, New York 11973

Received: November 8, 1995[⊗]

The structure of bromide adlayers at the Au(111)–aqueous solution interface has been studied by in-situ surface X-ray scattering (SXS) and scanning tunneling microscopy (STM). Both techniques show the existence of a hexagonal close-packed adlayer phase above a critical potential and are in good quantitative agreement on the adlayer structural parameters. The bromide–bromide spacing changes continuously between 4.24 Å at the critical potential and 4.03 Å at a potential 300 mV more positive. The adlayer is rotated relative to the substrate by an angle dependent on potential and bromide concentration. The potential-dependent adlayer density corresponding to these structural results agrees well with Br surface excess densities from published electrochemical measurements. At very positive potentials a bromide-induced step-flow etching of the Au substrate is observed. The results are used to compare the different techniques and to discuss the adlayer structure, the phase behavior, and the halide–gold chemical interaction.

1. Introduction

The adsorption of anions on metal electrodes is a major topic in interfacial electrochemistry and has been extensively studied by classical electrochemical methods. Of particular interest are chemisorbed (also called *contact adsorbed* or *specifically adsorbed*) anions, whose adsorption is controlled by both electronic and chemical forces. This results in complex adsorption isotherms and in high anionic surface excess densities at the most positive potentials. A typical example is the specific adsorption of chloride, bromide, and iodide. Adsorption isotherms of these anions on noble metals were measured over the past decades by electrochemical and spectroscopic techniques,^{1–7} quartz microbalance,⁸ and ex-situ vacuum techniques.^{9–11} In the past years, scanning probe and X-ray techniques have been used to investigate the structure of halide adlayers on Au,^{12–23} Pt,^{24–27} and Ag^{28,29} single-crystal electrodes in situ. These studies revealed a much richer phase behavior than previously anticipated, including the formation of non-primitive commensurate and incommensurate structures.

Up to now, most in-situ studies of halide adsorption investigated the structure of iodine adlayers, which are extremely strong chemisorbed on noble metals. This often hinders a simple thermodynamic interpretation. For example, considerable hysteresis between adsorption and desorption¹⁸ as well as coexistence of various adlayer structures over a larger potential range²⁴ has been observed. Hence, iodide adsorption on noble metals may not provide the ideal system to develop and test microscopic theories of specific adsorption. For bromide and chloride, in contrast, much more reversible adsorption isotherms are found, but only a few in-situ studies of the adlayer structure have been reported.^{12,27–29} Detailed structural data on bromide and chloride adlayers may promote a comprehensive understanding of halide adsorption and a more complete view of specific adsorption in general.

As will be demonstrated in the present study, the adsorption

of bromide on gold electrodes indeed provides an excellent model system for the study of these phenomena. Adsorption isotherms for bromide on gold have been obtained by various electrochemical and spectroscopic techniques,^{1,3,8,9,30} and in-situ STM observations of an ordered hexagonal Br layer on Au(111) have been reported by Tao and Lindsay.¹² However, experimental problems in the latter study prevented accurate measurements of the lattice parameters. As we will show, precise knowledge of the structural parameters is mandatory to fully characterize the phase behavior of adsorbed bromide. In addition, the phase behavior as a function of potential and bromide concentration is still unknown.

In this publication we give a detailed account of the results of bromide on Au(111) obtained by a combined SXS and STM study, which extends our recent brief report of the observation of ordered chloride and bromide adlayers on Au(111) by surface X-ray diffraction.³¹ In particular, we will show that the same potential-dependent structure of the adlayer is observed by both techniques and that the corresponding coverages agree well with recent electrochemical data. The paper is organized as follows. After presenting the experimental details (section 2) and the electrochemical behavior (section 3.1), the X-ray diffraction experiments are described in section 3.2. In section 3.3 the results of STM experiments are presented, which were performed for two reasons: first, to resolve differences between the X-ray diffraction data and results from prior STM studies¹² and, second, to study bromide-induced changes in the morphology of the Au substrate. SXS, STM, and recent electrochemical data of Shi and Lipkowski^{5,30} will be compared in section 4.1. The structure of the adlayer and the chemical interaction of bromide with Au electrodes will be discussed in sections 4.2 and 4.3, respectively.

2. Experimental Section

Cyclic voltammograms, X-ray diffraction, and STM experiments were carried out on the same Au(111) single-crystal electrodes in deaerated 0.1 M HClO₄ + *x* M NaBr solution with 10^{–1} ≥ *x* ≥ 10^{–4}.³² The single crystals were oriented along (111) with a miscut angle below 0.1°, mechanically polished, and electropolished in cyanide solution. Before each experiment

* Authors to whom correspondence should be addressed.

[†] New address: Olaf Magnussen, Abteilung Oberflächenchemie und Katalyse, University Ulm, 89069 Ulm, Germany.

[⊗] Abstract published in *Advance ACS Abstracts*, February 15, 1996.

the crystal was prepared by sputtering and annealing at 1000 K in vacuum or by flame-annealing and then transferred into the electrochemical environment. Solutions were made from high-purity HClO_4 (Merck, suprapur), high-purity NaBr (Aldrich, 99.999%), and Milli-Q water.

Cyclic voltammograms were obtained in deaerated electrolyte in the hanging meniscus geometry. The same Ag/AgCl (3 M KCl) reference electrode as in the SXS experiments was used.

Diffraction experiments were performed with monochromatic X-rays ($\lambda = 1.54 \text{ \AA}$) at the National Synchrotron Light Source at beamline X22B. The experimental procedures have been described previously^{18,33} and will be described here only briefly. The sample is mounted in an electrochemical thin-layer cell made from Kel-f with a Au counter and a Ag/AgCl reference electrode. The Au(111) surface faces a $4 \mu\text{m}$ thick Prolene (Chemplex) X-ray window. At the beginning of the experiment this window was inflated by filling the cell with deaerated electrolyte, resulting in a several millimeter thick liquid layer on top of the Au surface. For the X-ray measurements the liquid layer was reduced to $\approx 10 \mu\text{m}$ by deflating the cell. The electrochemical cell was enclosed in an outer cell filled with high-purity nitrogen gas. X-ray reflections are indexed according to the hexagonal coordinate system³³ formed by two vectors \vec{a} and \vec{b} to the nearest-neighbor atoms within the surface plane ($|\vec{a}| = |\vec{b}| = a_{\text{Au}} = 2.885 \text{ \AA}$) and one vector \vec{c} along the surface normal ($|\vec{c}| = 7.067 \text{ \AA}$). In section 3.2 only the first two components (H, K) of the corresponding reciprocal lattice are given, which describe the wavevector within the surface plane. The component L normal to the surface was usually kept at 0.2 (corresponding to a grazing incident angle of 1.25°). All structural data were obtained from fits of the diffraction peaks to a simple Gaussian (azimuthal scans) or to a Lorentzian line shape convoluted by a Gaussian resolution function with a half-width at half-maximum (hwhm) of 0.0057 \AA^{-1} (radial scans).

For the STM experiments a Nanoscope III instrument was used. Tunneling tips were etched from polycrystalline W wire and coated with nail polish. An electrooxidized Au wire served as a reference electrode. Due to chemical interaction with the electrolyte, the reference potential slowly drifts with time over the several hours required for the STM measurements. Hence, the potential scale was calibrated in situ at various stages of the measurement by the potential of Au dissolution (see section 3.1) and by the potential of ordered adlayer formation. All potentials are referred against Ag/AgCl . All presented images except Figure 6b, which is recorded in constant-height mode, are obtained in constant-current mode. The images are presented as top views with darker colors corresponding to lower height (or current) levels and are filtered by a low-pass filter only.

3. Results

3.1. Cyclic Voltammogram. Figure 1 shows a cyclic voltammogram of our Au(111) single crystal in deaerated 0.1 M $\text{HClO}_4 + 0.1 \text{ M NaBr}$ solution obtained in a separate electrochemical cell. Several features characteristic for bromide adsorption on Au(111) are observed, in good agreement with voltammograms reported in the literature.^{5,30,34} At -0.12 and -0.18 V we find peaks in the anodic and cathodic potential sweep. As shown before,^{30,33} these peaks are related to the lifting and re-formation of the Au surface reconstruction due to the adsorption and desorption of a few percent of bromide, respectively. The major change in bromide surface concentration occurs within this peak and a broad shoulder, i.e., in the potential range -0.2 to $+0.2 \text{ V}$. At more positive potentials (0.2 – 0.65 V) the current is almost constant but higher than the

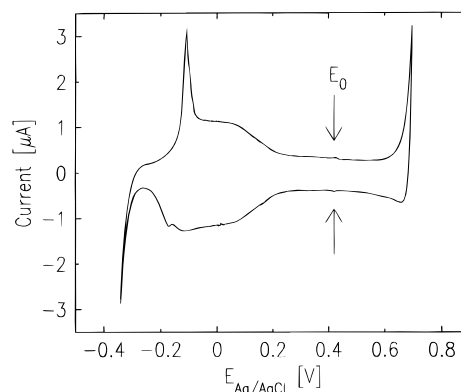


Figure 1. Cyclic voltammogram of Au(111) in 0.1 M $\text{HClO}_4 + 100 \text{ mM NaBr}$ (potential scan rate 10 mV/s).

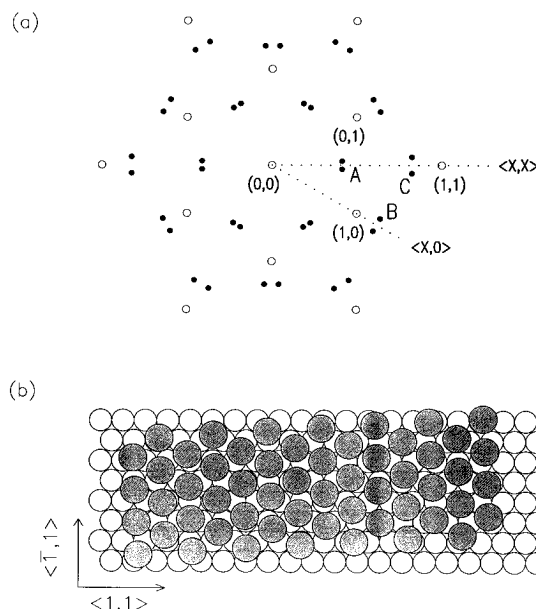


Figure 2. (a) X-ray diffraction pattern and (b) corresponding bromide surface structure. The positions of the crystal truncation rods of the Au(111) substrate (open circles) in (a) are indexed according to the hexagonal coordinate system. The first (A), second (B), and third (C) order diffraction peaks of the bromide adlayer (filled circles) are arranged in pairs with each peak rotated relative to Au peaks of the same order by $30^\circ \pm \phi$, where ϕ is a small potential-dependent angle. The real-space model in (b) shows one domain of the corresponding hexagonal adlayer (filled circles), which is rotated by ϕ relative to the $\sqrt{3}$ direction of the Au surface (open circles).

current at -0.25 V , where bromide is completely desorbed. This additional current is associated with further specific adsorption of bromide at a slower rate.³⁰ In this potential range a small and completely reversible peak is observed at 0.42 V in the anodic and cathodic potential scan (arrows). As will be shown subsequently, this peak is correlated with the formation of an ordered structure within the bromide adlayer. The corresponding peak potential will be called E_0 in the following. Above 0.65 V the current rapidly increases due to bromide oxidation and anodic dissolution of the Au substrate.

3.2. X-ray Diffraction Experiments. At potentials above 0.2 V the Au surface is unreconstructed, and in-plane diffraction peaks are only found at the positions of the crystal truncation rods. Changes are only observed if the potential is raised into the range positive of E_0 (i.e., above 0.42 V in solution with 0.1 M NaBr). The diffraction pattern in this potential range is shown in Figure 2a. It exhibits six hexagonally arranged pairs of diffraction peaks at the first-, second-, and third-order positions A, B, and C. As visible in the scattering profiles

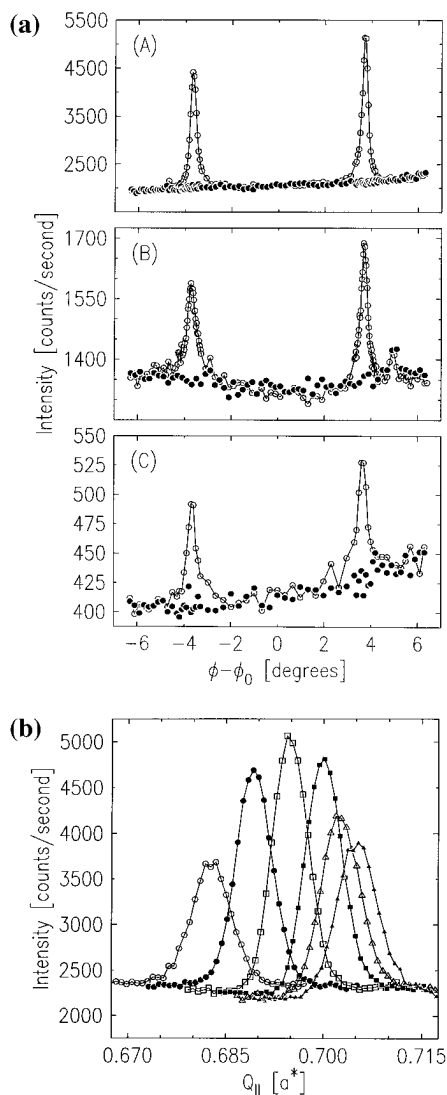


Figure 3. (a, top) Azimuthal scans at the positions of the superstructure peaks in 0.1 M HClO₄ + 10 mM NaBr at 0.2 V (filled circles) and 0.6 V (open circles). At 0.6 V diffraction peaks are observed, which are rotated by $\phi = \pm 3.7^\circ$ relative to $\phi_0 = 30^\circ$ ($\langle X, X \rangle$ direction) for (A) and (C) and $\phi_0 = 0^\circ$ ($\langle X, 0 \rangle$ direction) for (B). (b, bottom) Radial scans through the first bromide diffraction peak at 0.48 V (open circles), 0.52 V (closed circles), 0.56 V (open squares), 0.60 V (closed squares), 0.64 V (open triangles), and 0.68 V (closed triangles).

shown in Figure 3a, the peaks are rotated with respect to the $\langle X, X \rangle$ axis (A and C) and the $\langle X, 0 \rangle$ axis (B) by the same small angle ϕ . Rotation angle ϕ and radial peak position are a function of the potential and range from 3.2° to 4.7° for ϕ and from 0.683 to 0.716 for the position a_{Br}^* (in units of a_{Au}^*) of the first-order peak A, respectively. The potential dependence of the peak positions is illustrated by radial scans at various potentials shown in Figure 3b.

As described previously,¹⁸ this diffraction pattern indicates a rotated-hexagonal adlayer structure as shown in Figure 2b. The bromide adlayer is rotated by $\pm\phi$ relative to the $\sqrt{3}$ direction (i.e., to the $\langle \bar{1}, 1 \rangle$ axis in the hexagonal coordinate system) of the Au substrate. The nearest-neighbor distance a_{Br} of the adatoms in this ordered bromide monolayer ranges between 4.24 and 4.03 Å. The diffraction peaks have a hwhm of 0.15° – 0.3° in the azimuthal scans (see below) and a potential-independent hwhm of $0.003a_{Au}^*$ in the radial scans (Figure 3b). Assuming a perfect sample mosaic, this corresponds to a spatial coherence length of 330 Å.¹⁸ This is smaller than the coherence length of the underlying Au substrate (550 Å) but similar to

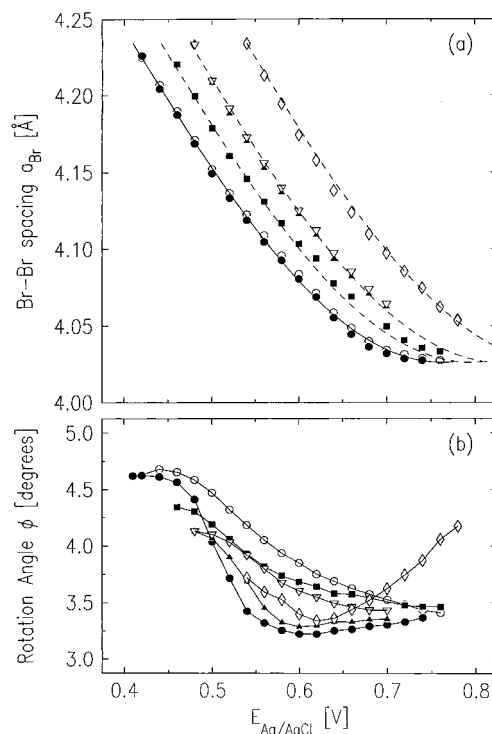


Figure 4. (a) Nearest-neighbor spacing $a_{Br}(E)$ and (b) rotation angle $\phi(E)$ relative to the Au $\sqrt{3}$ direction of the bromide adlayer on Au(111) in 0.1 M HClO₄ containing 100 mM (circles), 33 mM (squares), 10 mM (triangles), and 1 mM (diamonds) NaBr. Open and filled symbols correspond to the positive and negative direction of the potential sweep, respectively. $a_{Br}(E)$ data for 100 mM NaBr were fitted to a third-order polynomial resulting in $a_{Br}(E) = 4.5466 \text{ \AA} - 0.2545 \text{ \AA V}^{-1}E - 2.0264 \text{ \AA V}^{-2}E^2 + 1.9213 \text{ \AA V}^{-3}E^3$ (solid line); the $a_{Br}(E)$ curves at other concentrations are described by shifting this curve 32, 65, and 130 mV positively (dashed lines).

the coherence length observed for the rotated-hexagonal phase of iodide adlayers on Au(III).¹⁸

The dependence of the adatom–adatom spacing a_{Br} and the rotation angle ϕ on potential and bromide concentration is shown in Figure 4. They were obtained from experiments where the potential was changed stepwise by 20 mV every 370 s in positive (filled symbols) or negative (open symbols) direction. For NaBr concentrations between 10 and 100 mM the potential was first increased, starting from the potential of the ordered adlayer formation, and then decreased again (in 10 and 100 mM NaBr solution only). The $a_{Br}(E)$ values obtained in the positive and in the negative potential scan differ by less than 0.005 Å; i.e., the adatom–adatom spacing is a well-defined function of the potential. In 1 mM NaBr solution the kinetics of bromide adsorption is considerably decreased by the thin-layer geometry of the X-ray experiment, and only the curve in negative direction could be obtained (starting with a bromide adlayer which was adsorbed after inflating the cell at 0.78 V).

At the potential E_0 , where the ordered adlayer is formed, the adlattice spacing is 4.24 Å. With increasing potential the adlayer is compressed over a potential range of 300 mV down to a saturation value of 4.03 Å. This electrocompression of the adlayer is monotonic, and no discontinuities in the $a_{Br}(E)$ curves are observed. Hence, we can exclude a lock-in of the adlayer into high-order commensurate structures, which would result in a fixed bromide spacing in a certain potential regime. Numerically, the $a_{Br}(E)$ curves can be approximated by a third-order polynomial. A fit of the data in 100 mM NaBr solution to this functional form is shown as a solid line in Figure 4a; shifting this curve by 65 ± 3 mV per logarithm of NaBr concentration (dashed lines) provides an excellent description

of the data at lower concentrations. This potential shift is close to the 59 mV shift which is expected for a nominal charge transfer of $1 e^-$ from the bromide to the Au electrode, i.e., for an electroadsorption valency $\gamma = -1$.

While the $a_{Br}(E)$ curves are completely reversible, the potential dependence of the rotation angle $\phi(E)$ exhibits a more complicated behavior (Figure 4b). A nearly reversible $\phi(E)$ dependence is found only if the potential is maintained within ≈ 100 mV positive of E_0 . Changing the potential to more positive values, as in the experiments shown in Figure 4, results in a large hysteresis of up to 0.7° between the positive and the negative potential scan. In addition, the $\phi(E)$ dependence is different for different NaBr concentrations in the electrolyte. For example, $\phi(E_0)$ is 4.62° , 4.34° , 4.13° , and 3.72° in 100, 33, 10, and 1 mM NaBr solution, respectively, although the adlayer spacing $a_{Br}(E_0)$ has the same value of 4.24 \AA at all four concentrations. The nature of this shift in ϕ by $\approx 0.4^\circ$ per decade of NaBr concentration is not understood. Independent of Br concentration, ϕ approaches a saturation value of $\phi \approx 3.4^\circ$ at the most positive potentials in all experiments where the potential was increased slowly in small potential steps. This value is approximately maintained in the negative potential scan down to a potential ≈ 100 mV positive of E_0 , above which ϕ returns to a higher value. Only the $\phi(E)$ curve in 1 mM solution qualitatively differs from this behavior, in particular, at the positive end of the potential range where the value of ϕ is much higher. This is probably related to the different experimental procedure by which the most positive potential is approached (potential step at inflated cell instead of slow stepwise increase with deflated cell). It should be noted that even at this concentration ϕ decreases to 3.4° before it increases again.

The hysteresis in $\phi(E)$ is paralleled by distinct changes in the widths and intensities of the diffraction peaks. As an example, Figure 5 shows data of an experiment in 0.1 M NaBr solution, where the potential was first stepwise decreased from 0.5 to 0.4 V (filled triangles), then increased to 0.76 V (open circles), and finally decreased back to 0.4 V (filled circles). Parts b and c of Figure 5 show the hwhm $\Delta\phi(E)$ of the diffraction peaks along the azimuthal scan direction and the total integrated peak intensity, respectively. To illustrate the relationship between peak position and peak width, the figure (Figure 5a) includes the rotation angle $\phi(E)$, shown in Figure 4b, with error bars given by $\pm\Delta\phi(E)$. As seen in the figures, the hysteresis in $\phi(E)$ is paralleled by a hysteresis in $\Delta\phi(E)$ whereas the peak intensity changes in a reversible way over the entire potential range. A distinctly different behavior of $\Delta\phi(E)$ and the peak intensity is found for the potential region where $\phi(E)$ behaves nearly reversible and the region where $\phi(E)$ exhibits hysteresis. For potential changes within ≈ 100 mV of E_0 , $\Delta\phi(E)$ maintains a constant value of $\approx 0.15^\circ$. In this potential range the peak intensity changes almost linearly with potential and more than doubles between E_0 and 0.54 V. This potential dependence cannot be caused by changes in the coverage of the Br adsorbate, which varies only slightly with the potential (see below) but has to be explained otherwise. Either the ordering of the adlayer at E_0 occurs only on parts of the surface in form of islands, which coexist with disordered areas and grow with increasing potential, or the surface-normal distribution and the Debye-Waller factor of the adsorbates changes with potential. Differentiating between these two explanations would require measurements of the full adsorbate truncation rods at various potentials, which was not attempted. At 0.54 V the peak intensity approaches a constant, maximum value. Increasing the potential into this range causes a broadening of the peaks in azimuthal direction (see Figure 5a,b, open circles) up to a

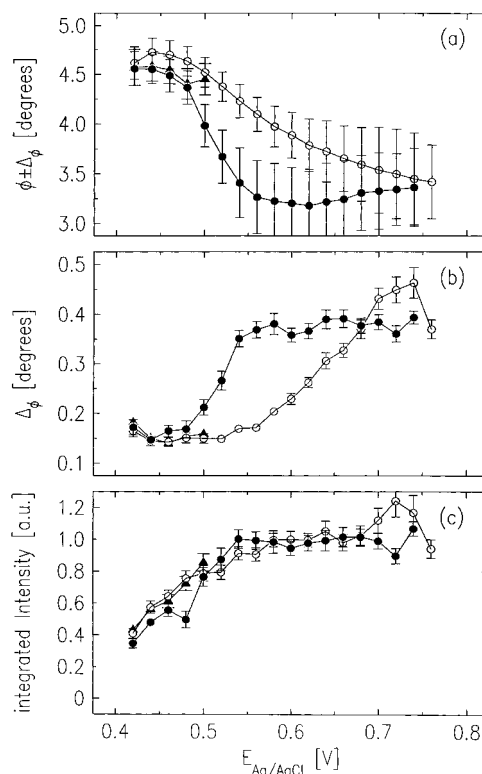


Figure 5. (a) Rotation angle $\phi(E)$, (b) azimuthal hwhm $\Delta\phi(E)$, and (c) integrated peak intensity (normalized to the saturation value) of the first-order diffraction peak of the bromide adlayer on Au(111) in 0.1 M HClO₄ + 100 mM NaBr, obtained from fits of azimuthal scans to a Gaussian. The potential was changed in 20 mV steps at a rate of 370 s/step from 0.5 to 0.4 V (filled triangles), then to 0.76 V (open circles), and then back to 0.4 V (filled circles). The error bars in (b) and (c) correspond to the instrumental errors; the error bars in (a) depict $\Delta\phi$ to illustrate the widths of the diffraction peaks.

$\Delta\phi(E)$ in the range 0.35° – 0.45° . It is noteworthy that the diffraction peaks in the azimuthal scans cannot be described perfectly by the Gaussian fits but seem to exhibit a broader tail toward lower angles ϕ (see Figure 3a). The broadening and the shift in position toward lower angles in this potential range may therefore be partly related to an increase in this low-angle tail. In addition, the non-Gaussian peak shape and the constant, potential-independent value of the fwhm along the radial direction indicate that the peak broadening is associated with a broader distribution of the local angle ϕ of the individual rotational domains rather than a change in the adlayer coherence length. Upon decreasing the potential (filled circles) significant changes in the peak position and width are observed only at potentials below 0.54 V, where $\phi(E)$ and $\Delta\phi(E)$ rapidly approach their reversible values. The microscopic origin of this complex behavior will be further discussed in section 3.3.

Finally, over the entire potential range no indication is found for other ordered adlayer structures. Particular closely studied was the potential range between 0.2 V and E_0 , where the bromide coverage is high and where the observation of a $(\sqrt{3} \times \sqrt{3})R30^\circ$ structure was reported.¹² In this range no additional peaks indicative of an ordered superstructure are observed along the $\langle X,0 \rangle$ and the $\langle X,X \rangle$ axis, ruling out the existence of a $(p \times \sqrt{3})$ phase, as observed for iodine on Au(111).¹⁸ In particular, no peaks at the $(1/3, 1/3)$ positions are found at any potential, which excludes the presence of a well-ordered $(\sqrt{3} \times \sqrt{3})R30^\circ$ structure. Below 0.2 V additional peaks corresponding to the formation of the Au(111) surface reconstruction are observed. The X-ray diffraction results on the

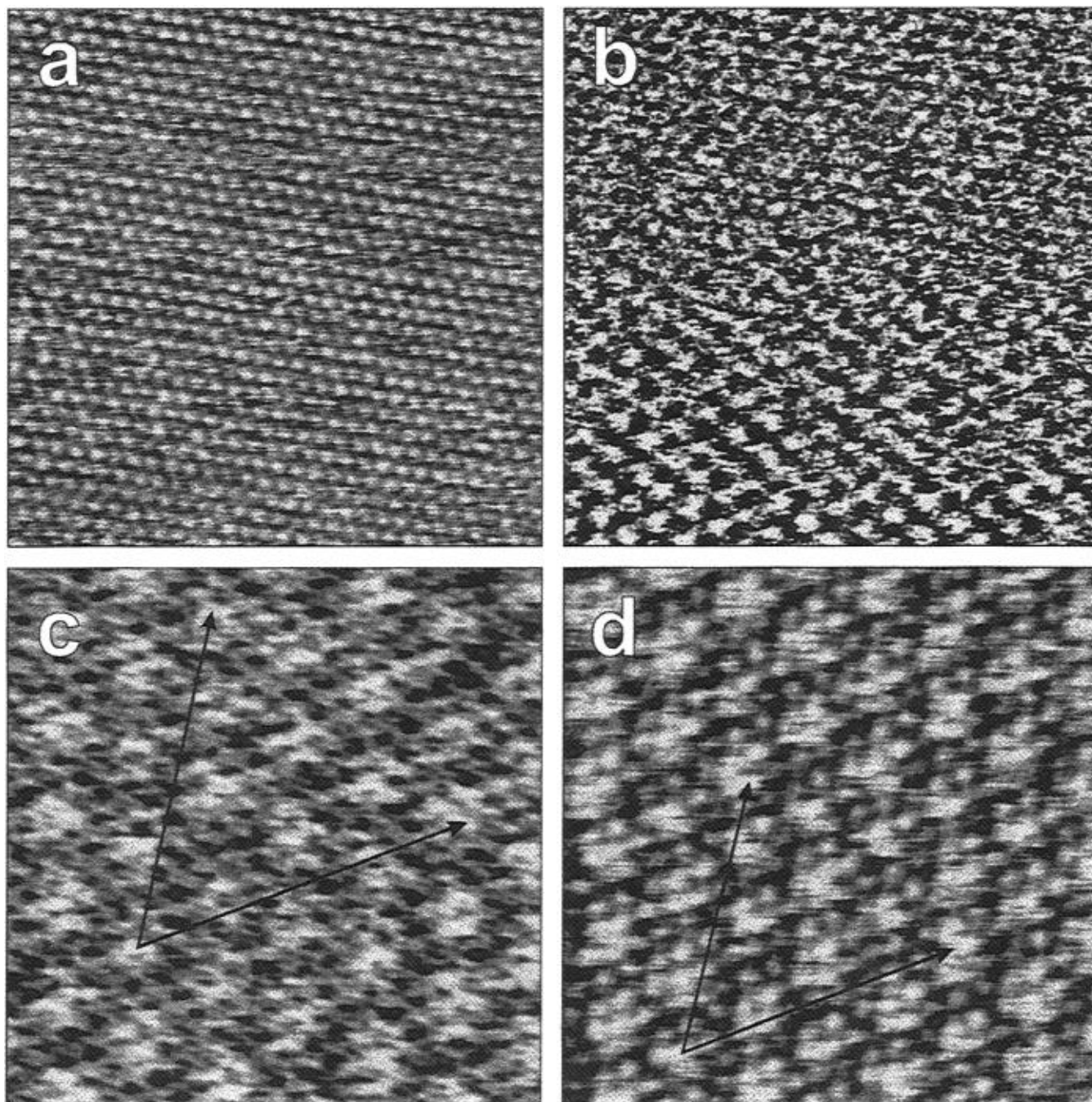


Figure 6. STM images of (a, c, d) $80 \times 80 \text{ \AA}^2$ and (b) $65 \times 65 \text{ \AA}^2$ large surface areas on Au(111) in 0.1 M $\text{HClO}_4 + 1 \text{ mM NaBr}$. (a) At 0.44 V only the hexagonal Au substrate lattice is visible; (b) upon increasing the potential with a sweep rate of 5 mV/s from 0.48 V (upper edge) to 0.59 V (lower edge) the rotated-hexagonal bromide adlayer is formed (center). Due to the different mismatch of the adlattice and the Au substrate at (c) 0.59 and (d) 0.74 V a slightly different long-range modulation pattern is observed in these images. By approximating the adlattice by high-order commensurate unit cells (arrows indicate unit cell vectors), the lattice parameters can be estimated (see text).

structural phase transition between the reconstructed and the unreconstructed surface in bromide solutions are described in ref 30 and will not be discussed here.

3.3. STM Experiments. Atomic scale STM images of the Au(111) surface in 1 mM NaBr solution are shown in Figure 6. At 0.44 V (Figure 6a) only a hexagonal lattice with a lattice spacing of 2.9 Å, congruent with the Au substrate lattice ($a_{Au} = 2.885 \text{ \AA}$), is visible although Br coverages of 0.2–0.3 monolayer can be estimated from coulometric experiments.⁵ As suggested before,³⁵ this apparent transparency of the anion adlayer may be caused by a high adsorbate mobility. The formation of the ordered bromide adlayer at more positive potentials can be observed in Figure 6b. In this experiment the potential was increased by 5 mV/s from 0.48 V (upper edge)

to 0.59 V (lower edge). In the upper half of the image the Au lattice can be clearly recognized. However, in the center this structure is replaced by a new hexagonal structure. The lattice of this superstructure has a larger spacing ($\approx 4.2 \text{ \AA}$) and is rotated relative to the Au lattice by $\approx 25^\circ$, which is in good agreement with the SXS results. This structure can be observed up to a potential of 0.8 V where the anodic dissolution of the Au starts (see below). If the potential is kept constant in the potential range of the ordered adlayer, the superstructure is always observed over the entire area imaged by the STM, and no coexisting disordered areas are visible. Nevertheless, the existence of such areas as suggested in section 3.2 cannot be excluded, since the STM's tip may stabilize the ordered phase in the scanned surface area.

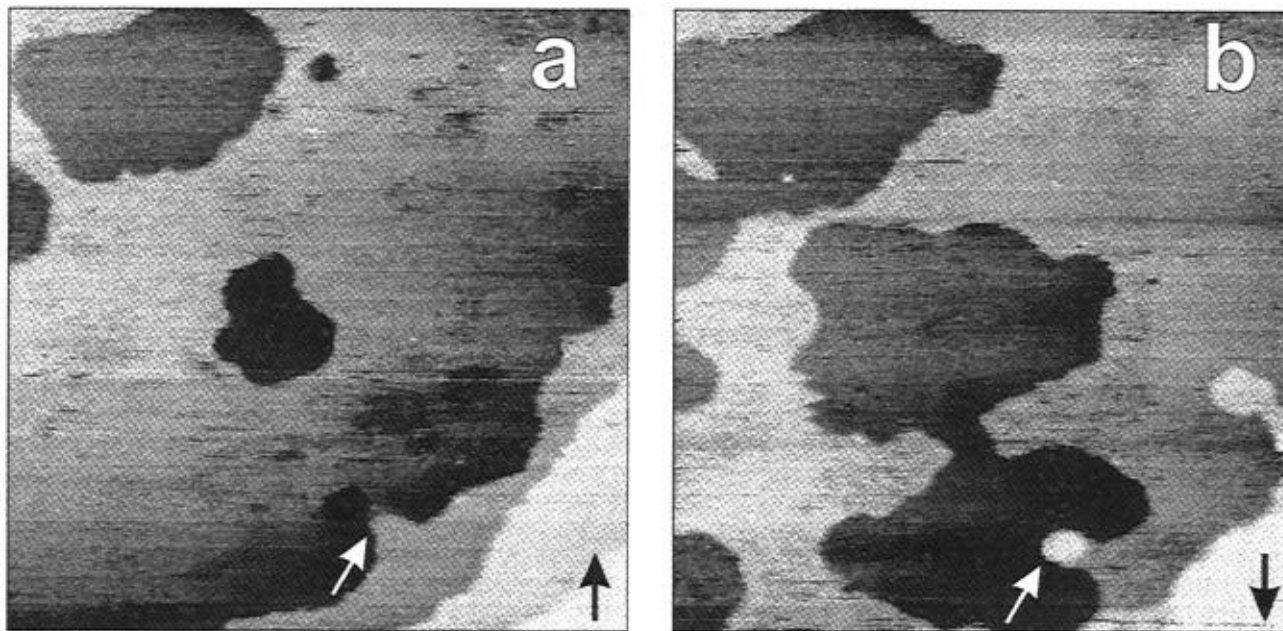


Figure 7. STM images of a $1000 \times 1000 \text{ \AA}^2$ large surface area on Au(111) in 0.1 M HClO₄ + 10 mM NaBr showing the anodic dissolution of Au by a step-flow etching mechanism. The images are recorded subsequently at a rate of 2 min/image 1 min after the potential was increased to 0.7 V; the slow scan direction is indicated by black arrows in the lower left corner (white arrows are described in the text).

The mismatch between substrate and adlattice creates a long-range modulation (Moiré pattern) which can be observed in high-resolution STM images such as Figure 6c,d. The long-range modulation pattern is very sensitive to the lattice mismatch a_{Br}/a_{Au} (and, hence, to the adlayer spacing a_{Br}) and the rotation angle ϕ . In the image in Figure 6c, recorded at 0.59 V, the modulation maxima repeat at a period of 13.3 Å. In contrast, the periodicity of the modulation in the more compressed adlayer at 0.74 V (Figure 6d) has decreased to 11.6 Å. The structural parameters of the Moiré pattern and a_{Br}/a_{Au} and ϕ are linked by a simple algebraic relationship,³⁶ which in principle could be used to calculate a_{Br} and ϕ . Measurements of angles and distances in STM images, however, are often imprecise due to thermal drift and imperfect calibration of the STM piezos. Much more precise structural data on a_{Br} and ϕ can be obtained by approximating the adlattice structure by a high-order commensurate structure with similar Moiré pattern. This technique does not require any absolute measurements and is therefore independent of image distortions.

Using this method, the structures in Figure 6c,d were approximated by $(\sqrt{301} \times \sqrt{301})R33.3^\circ$ and $(\sqrt{193} \times \sqrt{193})R33.3^\circ$ structures, respectively. (Unit cell vectors are indicated in the figures.) The lattice vector $\vec{a}_{commens}$ of these commensurate unit cells is parallel to \vec{a}_{Br} ; its length is given by the distance between maxima of the Moiré pattern along this direction ($12a_{Br}$ and $10a_{Br}$ for Figure 6, c and d, respectively). From this the adlattice spacing can be calculated, e.g., as $a_{Br} = \sqrt{301} \cdot 2.885/12 \text{ \AA}$ for the structure in Figure 6c; the relative error in a_{Br} is given by $\Delta/|\vec{a}_{commens}|$, where Δ is an estimate of the deviation from the commensurate position ($a_{Br} \gg \Delta \approx 0.5 \text{ \AA}$). The resulting parameters for the adlayer are $a_{Br} = 4.17 \pm 0.04 \text{ \AA}$ and $\phi = 3.3 \pm 0.5^\circ$ at 0.59 V and $a_{Br} = 4.01 \pm 0.04 \text{ \AA}$ and $\phi = 5.3 \pm 0.5^\circ$ at 0.74 V. In addition, experiments in 0.1 mM NaBr solution revealed a spacing of $a_{Br} = 4.17 \pm 0.04 \text{ \AA}$ at 0.66 V, which is consistent with a 60 mV potential shift per decade of concentration. These structural parameters for the rotated-hexagonal structure are in approximate agreement with those of previous in-situ STM experiments, which found $a_{Br} = 4.4 \text{ \AA}$ and $\phi = 10 \pm 3^\circ$.¹²

The etching of the Au(111) surface at very positive potentials is illustrated in Figure 7. The STM images in this figure were successively recorded in time intervals of 2 min in a surface area exhibiting originally a terrace with several monatomic deep holes (typical diameter $\approx 50 \text{ \AA}$) and a series of monatomic steps in the lower right corner. Figure 7a was recorded just after the potential was raised to the onset of the high positive current in the voltammogram (0.7 V in 10 mM NaBr solution). At this potential the sample topography changes continuously with time at a fast rate, and the STM, consequently, does not provide static images. Instead, the slow-scan direction now also serves a time scale. (Note that Figure 7a is recorded from bottom to top and Figure 7b from top to bottom.) As can be seen in Figure 7a and the subsequently recorded image in Figure 7b, the holes continuously increase in size and the step edges withdraw. In contrast, formation of etch pits in the center of an atomically flat terrace is not observed. Hence, the surface is etched only at step edges. The local rate of this step-flow etching can be estimated from the progression of the step edges with increasing time difference between the scan lines in the successive STM images (0 s difference at the upper edge of the images, 240 s at the lower edge). The steps move with 1–4 Å/s, which would give etch rates of 0.3–1.2 monolayer of Au per minute for an average step–step spacing of 200 Å. It should be noted that this is lower than the etch rate typically measured in macroscopic electrochemical experiments. First, typical (polycrystalline) Au electrodes usually have higher step densities, and second, the etch rate observed by STM may be limited by the slow diffusion of Br⁻ ions in the thin layer between tunneling tip and substrate.

Occasionally, the STM observations show local blocking of the step-flow etching. An example is found at the lower edge of Figure 7. Here a protrusion in the first step edge in Figure 7a survives as an isolated circular island in Figure 7b (see white arrows), while a whole monolayer has been removed in its immediate vicinity. The etch front which started in the center of the image (central hole) is separated by this island in two arms progressing to the left and the right. A similar feature is observed at the right edge of Figure 7b. These islands are probably caused by the pinning of strongly adsorbed impurities.

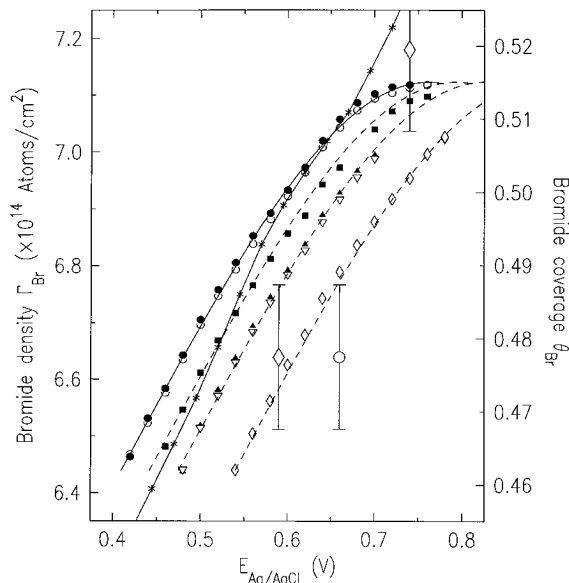


Figure 8. Surface concentration $\Gamma_{Br}(E)$ and coverage $\theta_{Br}(E)$ relative to the Au(111) surface density obtained by X-ray diffraction, STM, and chronocoulometry. SXS results in 0.1 M HClO₄ with 100 mM (circles), 33 mM (squares), 10 mM (triangles), and 1 mM NaBr are calculated from the data in Figure 4a; results of STM experiments in 0.1 M HClO₄ with 1 mM (large diamonds) and 0.1 mM (large circle) NaBr are calculated from the data given in section 3.3. For comparison, chronocoulometric data for 0.1 M KClO₄ + 1 mM HClO₄ + 1 mM KBr (stars) from ref 5 are shown (with permission of J. Lipkowski).

They locally conserve the original vertical position of the surface and may evolve to sharp protrusions with heights of many atomic layers after prolonged etching, thereby increasing the roughness of the surface.

4. Discussion

4.1. Comparison of Structural and Thermodynamic Data.

The results of our STM and SXS experiments are in good agreement. This is illustrated in Figure 8 which shows the surface concentration $\Gamma_{Br}(E)$ and the coverage relative to the Au substrate $\theta_{Br}(E)$, both calculated from the adatom spacing $a_{Br}(E)$. Taking into account the small uncertainty in the potential of the reference electrode for the STM experiments (≈ 30 mV), the $\Gamma_{Br}(E)$ data in 1 mM NaBr solution obtained by STM and by SXS measurements overlap within the experimental error. In particular, both techniques find an electrocompression of similar magnitude. However, the STM experiments examine the surface on a very local scale while SXS probes the surface structure within a coherence length (which exceeds the inverse resolution of $1/0.0057 \text{ \AA} = 175 \text{ \AA}$) incoherently averaged over a surface area of several mm². Hence, the good agreement indicates a very homogeneous adlayer structure without large spatial deviations. In addition, the very uniform appearance of the adlayer in the STM images demonstrates a high homogeneity on a very local scale. This, as well as the absence of satellite peaks and the continuous compression of the adlayer with potential, excludes an interpretation of the SXS results in terms of a local $(\sqrt{3} \times \sqrt{3})R30^\circ$ structure with a very high density of domain boundaries as had been suggested for similar incommensurate adlayer structures, e.g., for physisorbed noble gases,³⁷ and supports interpretation in terms of a true incommensurate phase.

Previous Br adlayer density measurements by specular X-ray reflectivity³³ agree well with the in-plane X-ray scattering results. Here a Br coverage of 0.49 or a surface density of 6.8×10^{-14} atoms/cm², localized in a single adlayer, was found in

the potential range of the rotated hexagonal adlayer structure (at 0.5 V in 0.01 M KBr). Since reflectivity measurements probe the density profile along the surface normal averaged within the surface plane, this measurement of the local coverage is independent of the in-plane order in the adlayer. Hence, the overall bromide adlayer density is the same as that measured by SXS for the ordered phase. In addition, the reflectivity data indicate an adlayer corrugation amplitude which is in good agreement with the corrugation amplitude calculated for the geometric modulation of the Moiré pattern. The Moiré corrugation amplitude obtained from the STM experiments, in contrast, is significantly smaller, probably due to electronic contributions in the STM image.

The rotated-hexagonal structure is the only ordered adlayer superstructure which was observed in our SXS as well as in our STM experiments. In contrast, previous STM experiments reported an additional $(\sqrt{3} \times \sqrt{3})R30^\circ$ superstructure in the potential range negative of the rotated-hexagonal adlayer.¹² This observation is at variance not only with our results but also with measurements of the coverage by chronocoulometry,⁵ quartz microbalance,⁸ and ex-situ electron spectroscopy,⁹ which find considerably higher Br coverages than the $1/3$ monolayer associated with a $(\sqrt{3} \times \sqrt{3})R30^\circ$ structure. Furthermore, no sharp spikes in the cyclic voltammogram, indicative of the formation of an ordered adlayer, are observed at lower potentials.

Finally, we compare our structural data to the bromide surface excess obtained by chronocoulometric experiments of Shi and Lipkowski⁵ (stars in Figure 8). By combining thermodynamic and structural information, a very detailed picture of bromide adsorption arises. Over a large potential range the results of the electrochemical and of the X-ray measurements differ by only 1–2%. (The larger deviation above 0.7 V is probably related to the onset of Au corrosion.) The good agreement of macroscopic and microscopic coverage measurements suggests that the majority of the adsorbed bromide is confined to a close-packed, ordered adlayer, and the amount of bromide anions in the diffuse layer is negligible.

Chronocoulometric experiments can measure the surface concentration $\Gamma_{Br}(E)$ in the potential range where the bromide adlayer is disordered and the structural probes are insensitive to the adsorbate. These measurements show that the formation of the ordered structure is not accompanied by a sudden uptake of bromide anions from the solution. Instead, $\Gamma_{Br}(E)$ increases continuously in the potential regime of the phase transition with the same slope $\partial\Gamma_{Br}/\partial E$ in the ordered and in the disordered phase. The potential regime where the Au surface is covered by a disordered adlayer with a similar compressibility as in the ordered phase starts at a potential 300 mV more negative than the potential of the disorder–order transition. It is preceded by a 300 mV wide potential regime where the major uptake of bromide occurs and the average increase $\partial\Gamma_{Br}/\partial E$ is about 7 times larger as in the ordered phase. This phase may be characterized as a two-dimensional gas in contrast to the more liquidlike behavior of the adlayer (high density, low compressibility, no long-range order) at more positive potentials. The 2D gas phase is correlated with the broad peak in the cyclic voltammogram and may be interpreted as Frumkin's adsorption of strongly repulsively interacting (partly charged) adsorbates.

4.2. Adlayer Structure. The coalescence of results from various techniques provides reliable data on the structural properties of the bromide adlayer, namely, the adlayer compressibility and orientation. These will now be discussed. We will occasionally refer to the results for similar close-packed adlayers of chloride³¹ and iodide¹⁸ on Au(111); an explicit comparison of all three halides can be found in ref 31.

According to our data, bromide forms an incommensurate adlayer structure on Au(111) rather than a series of high-order commensurate structures. This is indicated by the continuous change of the structure with potential as well as by the poorly defined adlayer orientation (see below). The best low-order commensurate approximation of the adlayer structure is a $(2\sqrt{7} \times 2\sqrt{7})R19.1^\circ$ structure with 13 bromide adatoms per unit cell and with $a_{Br} = 4.23 \text{ \AA}$ and $\phi = 3.0^\circ$. This structure resembles the structure observed at the potential of ordered adlayer formation ($a_{Br}(E_0) = 4.23 \text{ \AA}$), which may help trigger the initial ordering of the adlayer. The more close-packed structures at higher potentials, including the saturation structure above 0.7 V, could only be approximated by commensurate structures with unreasonably large unit cells (see Section 3.3). In principle, the compression of the adlayer at higher potentials could be also explained by a $(2\sqrt{7} \times 2\sqrt{7})R19.1^\circ$ structure, which becomes more condensed by the growth of heavy domain walls.³⁷ However, the constant hwhm of the diffraction peaks and the STM observations rule out this domain wall model.

In contrast to the adlayer spacing, the orientation of the bromide adlayer relative to the gold substrate is not a very well-defined quantity. It depends not only on the mismatch between the adlattice and the substrate lattice but also on the bromide concentration and the history of the potential changes. Apparently, the rotation angle ϕ is defined by a rather shallow minimum in the adlayer free energy. The nonequilibrium phase behavior of the rotation angle ϕ cannot be described by simple theories, such as that of Novaco and McTague.³⁸ Even at the most negative potentials, where the potential dependence of ϕ is reversible (for a given NaBr concentration), ϕ does not depend linearly on the incommensurability parameter $z = \sqrt{3\theta}$, as predicted by this theory. The structural identical, rotated-hexagonal iodide adlayer on Au(111), in contrast, is described well by the Novaco–McTague theory.¹⁸

Although the adlayer orientation cannot be described quantitatively, the following two observations seem noteworthy. First, the complicated, irreversible behavior of $\phi(E)$ in no way affects the potential dependence of the adlayer spacing $a_{Br}(E)$, which is a well-defined, smooth function over the entire potential range. This indicates that the adlayer structure is governed almost exclusively by the adsorbate–adsorbate interactions. The adlayer orientation can be regarded as a secondary effect, resulting from the best match of a fixed, rigid adlattice to the substrate lattice. Second, similar nonequilibrium behavior of the adlayer orientation has been observed in other adsorbed monolayers with similar structure. Examples are monolayers of iodide¹⁸ and Tl³⁹ on Au(111) and of Tl on Ag(111),⁴⁰ where the irreversibility in $\phi(E)$ was attributed to adsorbed impurities. In all these experiments the adlattice spacing was a well-defined function of potential. For I on Au(111) the experiments demonstrated the coexistence of two orientational phases differing by 0.2° in $\phi(E)$ over a 50 mV wide potential regime.¹⁸ A similar effect could account for the asymmetry in the azimuthal diffraction profiles observed for the ordered bromide adlayer. The potential dependence of ϕ could be explained by a model in which the orientation changes between two equilibrium states given by $\phi(E_0)$ at potentials close to E_0 and by $\phi \approx 3.4^\circ$ at more positive potentials. The transition between these states could be hindered by kinetic limitations resulting in the observed hysteresis.

The lateral two-dimensional compressibility of the adlayer is given by $\kappa_{2D} = \sqrt{3}z^{-1}e^{-1}a_{Br}(\partial a_{Br}/\partial E)$.^{40,41} For bromide on Au(111) κ_{2D} changes continuously from $6.74 \text{ \AA}^2 \text{ eV}^{-1}$ at the potential of ordered adlayer formation to $2.75 \text{ \AA}^2 \text{ eV}^{-1}$ over a potential region of 250 mV. (At higher potentials, where step

flow etching occurs, a_{Br} saturates and, consequently, $\kappa_{2D} \rightarrow 0$.) Hexagonal ordered chloride ($\kappa_{2D}(\text{Cl}) = 4.65 \text{ \AA}^2 \text{ eV}^{-1}$) and iodide ($\kappa_{2D}(\text{I}) = 5.40 \text{ \AA}^2 \text{ eV}^{-1}$) adlayers on Au(111)³¹ have compressibilities in the same range but vary less since their potential range of stability is smaller. In contrast, the compressibilities of metal monolayers formed by underpotential deposition^{40,41} are lower ($\kappa_{2D} \approx 1\text{--}2 \text{ \AA}^2 \text{ eV}^{-1}$)^{40,41} and those of physisorbed noble gases on metal surfaces are considerably higher ($\kappa_{2D} \approx 10\text{--}30 \text{ \AA}^2 \text{ eV}^{-1}$),^{42–44} in accordance with the expected hardness of the respective ion cores. A quantitative explanation of the compressibility of halide adlayer is difficult due to the complicated and unknown interatomic potentials involved. Calculations not only would require reliable data on the bromide–bromide interatomic potential but also would have to account for Coulombic and substrate-induced contributions and multi-particle interactions.

Our results on electrochemical halide adsorption show similar trends as previous studies of halide adsorption from the gas phase, which revealed the formation of ordered chemisorbed adlayers on a number of metal substrates.^{45,46} Although gas phase adsorption of bromine on Au(111) has not been studied explicitly, incommensurate close-packed adlayers structures with similar packing densities were observed in a vacuum environment for a number of other halide–metal systems. In addition, the packing density in those structures often changed uniformly with coverage, analogous to the electrocompressible structures observed at the solid–electrolyte interface. This structural agreement suggests an overall agreement in the chemical nature of the adlayers formed under halogen gas or in halide solution. Assuming that the presence of the bulk liquid phase is negligible, electrochemical and ultrahigh-vacuum studies of halide adsorbates on metal surfaces may complement each other. While the gas phase studies benefit from the availability of a wide variety of surface-sensitive techniques, experiments at the electrochemical interface allow studies of the strongly bound halide adsorbates under equilibrium conditions. Hence, the former can provide insight into electronic structure and binding; the latter give equilibrium structural parameters as a function of chemical potential.

4.3. Au–Br Surface Chemistry. In the following, we will describe briefly how the structural data are related to the halide–gold surface chemistry in aqueous solution. Previous reflectivity measurements indicated a spacing of 2.4 \AA between the adsorbate and the Au surface layer³³ for chloride, bromide, and iodide. This is close to the covalent bonding distance, although the incommensurate nature of the adlayer requires a more complicated, delocalized bonding. In contrast, the halide–halide spacing in the adlayer is close to the van der Waals diameter for all three species, similar as in bulk gold–halide compounds. This asymmetry in lateral and vertical bonding distances is not observed if the adsorbate–adsorbate and adsorbate–substrate interactions are similarly strong, as for example in close-packed adlayers of metals on metal electrodes.^{39,47} Hence, the bonding distances can be directly related to the different chemical interactions at the interface.

The adlayer is a precursor for the formation of soluble gold–halide complexes (AuX_2^- , AuX_4^- , $\text{X} = \text{Cl}, \text{Br}, \text{I}$) at positive potentials. For bromide, this process seems to involve (at least at the most negative potentials) merely the lower coordinated Au atoms at step edges, and the close-packed adlayer within the atomically flat terraces is unchanged. A similar step-flow etching mechanisms has been observed in chloride solutions,⁴⁸ whereas formation of triangular pits was observed upon chemical etching in cyanide solution.⁴⁹ The observed microscopic mechanism has two important practical consequences for the

etching of gold by bromide: First, the macroscopic etch rate and the homogeneity of the etched surface will depend strongly on the electrode microstructure. On polycrystalline surfaces, (111)-oriented surfaces will be etched considerably slower than less densely packed or highly stepped surfaces, which may induce faceting. Second, insoluble adsorbates on the surface such as organic impurities can hinder the movement of steps across the surface. In contrast to mechanisms involving the formation of etch pits, only a small fraction of the surface area, namely, the step edges, have to be blocked by adsorbates to drastically reduce the etching. In addition, partial blocking by adsorbates may cause selective etching, resulting in high surface roughness. The influence of blocking by adsorbed impurities should decrease with increasing halide-gold interaction. Indeed, the blocking effects observed in solutions containing chloride ions are much stronger than those in solutions containing bromide.⁴⁸

5. Conclusions

We have presented a detailed in-situ X-ray diffraction and STM study of the structure of bromide adlayers at the Au(111)-aqueous solution interface and compared it with previous electrochemical measurements.⁵ The good agreement of the results illustrates how these different techniques can be combined to get a comprehensive understanding of electrochemical chemisorption. The combined thermodynamic and structural data suggest a single adlayer of adsorbed bromide on the electrode surface, which proceeds with increasing potential from a two-dimensional gaslike via a two-dimensional fluidlike phase to an ordered, hexagonal close-packed monolayer. The ordered adlayer is incommensurate with the substrate, rotated versus the $\sqrt{3}$ direction by a small potential-dependent angle, and compresses monotonically over a potential range of about 300 mV. At even higher potentials bromide induces etching of the gold surface via a step-flow mechanism.

Acknowledgment. The authors thank J. Lipkowski for helpful and stimulating discussions and for providing coulometric data. This work was supported by the Divisions of Material and Chemical Sciences, U.S. Department of Energy, under Contract DE-AC02-76CH00016.

References and Notes

- (1) Adzic, R. R.; Yeager, E. B.; Cahan, B. D. *J. Electroanal. Chem.* **1977**, *85*, 267.
- (2) van Huong, C. N.; Hinnen, C.; Rousseau, A. *J. Electroanal. Chem.* **1983**, *151*, 149.
- (3) Sedlmaier, H. D.; Plieth, W. J. *J. Electroanal. Chem.* **1984**, *180*, 219.
- (4) Valette, G. *J. Electroanal. Chem.* **1988**, *255*, 215.
- (5) Shi, Z.; Lipkowski, J. *J. Electroanal. Chem.* **1994**, *369*, 283.
- (6) Shi, Z.; Wu, S.; Lipkowski, J. *Electrochim. Acta* **1995**, *40*, 9.
- (7) Gao, X.; Weaver, M. J. *J. Phys. Chem.* **1986**, *90*, 4057.
- (8) Deakin, M. R.; Li, T. T.; Melroy, O. R. *J. Electroanal. Chem.* **1988**, *243*, 343.
- (9) Kolb, D. M.; Rath, D. L.; Wille, R.; Hansen, W. N. *Ber. Bunsen-Ges. Phys. Chem.* **1983**, *87*, 1108.
- (10) Hubbard, A. T. *Chem. Rev.* **1988**, *88*, 633.
- (11) Zei, M. S. *J. Electroanal. Chem.* **1991**, *308*, 295.
- (12) Tao, N. J.; Lindsay, S. M. *J. Phys. Chem.* **1992**, *96*, 5213.
- (13) Haiss, W.; Sass, J. K.; Gao, X.; Weaver, M. J. *Surf. Sci.* **1992**, *274*, L593.
- (14) Gao, X.; Weaver, M. J. *J. Am. Chem. Soc.* **1992**, *114*, 8544.
- (15) Gao, X.; Weaver, M. J. *Phys. Rev. Lett.* **1994**, *73*, 846.
- (16) Gao, X.; Edens, G. J.; Weaver, M. J. *J. Phys. Chem.* **1994**, *98*, 8074.
- (17) Gao, X.; Edens, G. J.; Liu, F.-C.; Hamelin, A.; Weaver, M. J. *J. Phys. Chem.* **1994**, *98*, 8086.
- (18) Ocko, B. M.; Watson, G. M.; Wang, J. *J. Phys. Chem.* **1994**, *98*, 897.
- (19) Wang, J.; Watson, G. M.; Ocko, B. M. *Physica A* **1993**, *200*, 679.
- (20) Ocko, B. M.; Wang, J. In *Synchrotron Techniques in Interfacial Electrochemistry*; Melendres, C. A., Tadjeddine, A., Eds.; Kluwer Academic Press: Dordrecht, 1994.
- (21) Ocko, B. M.; Magnussen, O. M.; Wang, J. X.; Adzic, R. R. In *Nanoscale Probes of the Solid/Liquid Interface*; Gewirth, A. A., Siegenthaler, H., Eds.; Kluwer Academic Publishers: Dordrecht, 1995; Vol. E288, p 103.
- (22) Ocko, B. M.; Magnussen, O. M.; Wang, J.; Adzic, R. R.; Wandlowski, T. *Physica B*, in press.
- (23) Yamada, T.; Batina, N.; Itaya, K. *Surf. Sci.* **1995**, *335*, 204.
- (24) Yau, S.-L.; Vitus, C. M.; Schardt, B. C. *J. Am. Chem. Soc.* **1990**, *112*, 3677.
- (25) Vogel, R.; Baltruschat, H. *Ultramicroscopy* **1992**, *42-44*, 562.
- (26) Vogel, R.; Baltruschat, H. *Surf. Sci.* **1991**, *259*, L739.
- (27) Bittner, A. M.; Wintterlin, J.; Beran, B.; Ertl, G. *Surf. Sci.* **1995**, *335*, 291.
- (28) Aloisi, G.; Funtikov, A. M.; Will, T. *J. Electroanal. Chem.* **1994**, *370*, 297.
- (29) Foresti, M. L.; Aloisi, G.; Innocenti, M.; Kobayashi, H.; Guidelli, R. *Surf. Sci.* **1995**, *335*, 241.
- (30) Ocko, B. M.; Magnussen, O. M.; Adzic, R. R.; Wang, J.; Shi, Z.; Lipkowski, J. *J. Electroanal. Chem.* **1994**, *376*, 35.
- (31) Magnussen, O. M.; Ocko, B. M.; Adzic, R. R.; Wang, J. *Phys. Rev. B* **1995**, *51*, 5510.
- (32) Perchloric acid was added only to enhance the electrolyte conductivity at low bromide concentrations. Experiments in pure NrBr give identical results.
- (33) Wang, J.; Ocko, B. M.; Davenport, A. J.; Isaacs, H. S. *Phys. Rev. B* **1992**, *46*, 10321.
- (34) Scherson, D. A.; Kolb, D. M. *J. Electroanal. Chem.* **1984**, *176*, 353.
- (35) Magnussen, O. M.; Hageböck, J.; Hotlos, J.; Behm, R. *J. Faraday Discuss.* **1992**, *94*, 329.
- (36) Toney, M. F.; Gordon, J. G.; Borges, G. L.; Melroy, O. R. *Phys. Rev. B* **1994**, *49*, 7793.
- (37) Shiba, H. *J. Phys. Soc. Jpn.* **1979**, *46*, 1852.
- (38) McTague, J. P.; Novaco, A. D. *Phys. Rev. B* **1979**, *19*, 5299.
- (39) Wang, J.; Adzic, R. R.; Ocko, B. M. *J. Phys. Chem.* **1994**, *98*, 7182.
- (40) Toney, M. F.; Gordon, J. G.; Samant, M. G.; Borges, G. L.; Melroy, O. R.; Yee, D.; Sorensen, L. B. *Phys. Rev. B* **1992**, *45*, 9362.
- (41) Melroy, O. R.; Toney, M. F.; Borges, G. L.; Samant, M. G.; Kortright, J. B.; Ross, P. N.; Blum, L. *J. Electroanal. Chem.* **1989**, *258*, 403.
- (42) Unguris, J.; Bruch, L. W.; Moog, E. R.; Webb, M. B. *Surf. Sci.* **1979**, *87*, 415.
- (43) Unguris, J.; Bruch, L. W.; Moog, E. R.; Webb, M. B. *Surf. Sci.* **1981**, *109*, 522.
- (44) Kern, K.; Comsa, G. In *Chemistry and Physics of Solid Surfaces VII*; Vanselow, R., Howe, R., Eds.; Springer: Berlin, 1988; Vol. VII, p 65.
- (45) Farrell, H. H. In *The Chemical Physics of Solid Surfaces and Heterogeneous Catalysis*; King, D. A., Woodruff, D. P., Eds.; Elsevier: New York, 1984; Vol. 36, p 226.
- (46) Dowben, P. A. *CRC Crit. Rev. Solid State Mater. Sci.* **1987**, *13*, 191.
- (47) Samant, M. G.; Borges, G. L.; Melroy, O. R. *J. Electrochem. Soc.* **1993**, *140*, 421.
- (48) Möller, F.; Magnussen, O. M.; Behm, R. J. Unpublished results.
- (49) McCarley, R. L.; Bard, A. J. *J. Phys. Chem.* **1992**, *96*, 7410.